nature chemistry

Article

https://doi.org/10.1038/s41557-024-01556-3

Coherent photoexcitation of entangled triplet pair states

Received: 23 October 2023

Accepted: 13 May 2024

Published online: 19 June 2024

Check for updates

Juno Kim[1,6], David C. Bain[1,6], Vivian Ding[1], Kanad Majumder[2], Dean Windemuller[3], Jiaqi Feng[4], Jishan Wu[4], Satish Patil[2], John Anthony[3], Woojae Kim[5] ✉ & Andrew J. Musser[1] ✉

The functional properties of organic semiconductors are defined by the interplay between optically bright and dark states. Organic devices require rapid conversion between these bright and dark manifolds for maximum efficiency, and one way to achieve this is through multiexciton generation ($S_1 \rightarrow {}^1TT$). The dark state ${}^1TT$ is typically generated from bright S_1 after optical excitation; however, the mechanistic details are hotly debated. Here we report a ${}^1TT$ generation pathway in which it can be coherently photoexcited, without any involvement of bright S_1. Using <10-fs transient absorption spectroscopy and pumping sub-resonantly, ${}^1TT$ is directly generated from the ground state. Applying this method to a range of pentacene dimers and thin films of various aggregation types, we determine the critical material properties that enable this forbidden pathway. Through a strikingly simple technique, this result opens the door for new mechanistic insights into ${}^1TT$ and other dark states in organic materials.

The canonical picture of organic semiconductor photophysics is built on the dichotomy between bright and dark electronic states, defined by their optical accessibility/inaccessibility from the ground state. Whether the aim is to produce dark states like charge carriers in organic photovoltaics or to suppress or harvest dark states like triplets in organic light-emitting diodes, efforts to understand and control the interplay between bright and dark manifolds are at the heart of molecular optoelectronics[1–4]. Numerous factors can cause a state to be dark, such as molecular orbital overlap, symmetry, spin multiplicity and the coupling strength to vibrations or between electronic states, but, regardless, optical access requires the mediation of a bright (typically singlet) state[5]. An increasingly important pathway between these manifolds is singlet fission (SF) and its reverse, triplet–triplet annihilation, which convert between a singlet and a pair of dark triplets[6–9]. The essential gateway state in this process is itself dark, the spin-entangled triplet pair state ${}^1TT$[10–13]. ${}^1TT$ has garnered a great deal of attention for its applications in photovoltaic exciton multiplication schemes or—through spin evolution into ${}^5TT$—its potential as a high-temperature qudit for quantum information science[14–18].

The formation of ${}^1TT$ through SF can be extremely rapid (<100 fs), despite the state being optically dark and generally unable to couple strongly to the bright singlet S_1, and the detailed mechanism of this process is actively debated[19,20]. Two-photon photoelectron spectroscopy has established a model of coherent SF in which ${}^1TT$ could be directly photoexcited in a coherent superposition with S_1 due to strong electronic coupling (>50 meV), despite its optically dark nature[20]. Later optical spectroscopy suggested that the rapid SF could be explained by strong vibronic coupling, although this model could not explain the instantaneous appearance of apparent ${}^1TT$ signatures in the photoelectron spectroscopy results[21–23]. Recently, challenging orbital-resolved photoelectron spectroscopy has provided a new interpretation for these signatures as the hallmark of substantial charge-transfer (CT) character within the initial S_1 state[19]. This picture, in which coupling via CT states provides the bridge to enable rapid transfer from bright S_1 to dark ${}^1TT$, stands as the current consensus and is in line with

[1]Department of Chemistry and Chemical Biology, Cornell University, Ithaca, NY, USA. [2]Solid State and Structural Chemistry Unit, Indian Institute of Sciences, Bangalore, Republic of India. [3]Center for Applied Energy Research, University of Kentucky, Lexington, KY, USA. [4]Department of Chemistry, National University of Singapore, Singapore, Republic of Singapore. [5]Department of Chemistry, Yonsei University, Seoul, Republic of Korea. [6]These authors contributed equally: Juno Kim, David C. Bain. ✉e-mail: woojae@yonsei.ac.kr; ajm557@cornell.edu

https://doi.org/10.1038/s41557-024-01556-3

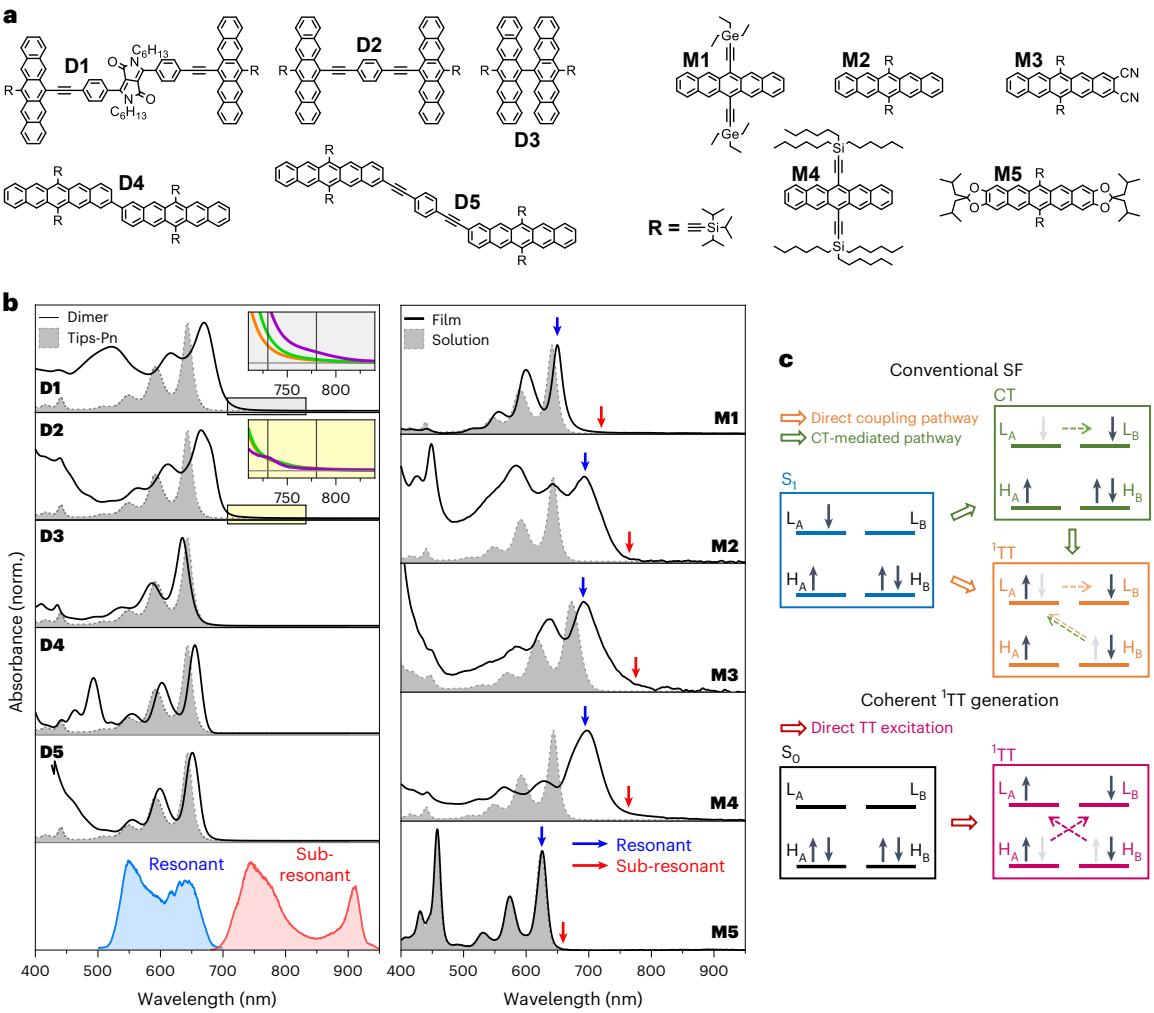

Fig. 1 | Structures and absorption spectra of pentacene derivatives. **a**, Structures of pentacene dimers **D1**–**D5** and monomers **M1**–**M5**. **b**, Steady-state absorbance spectra of the pentacene derivatives. Left: **D1**–**D5** absorbance spectra in THF (black lines), with an absorbance spectrum of Tips-Pn solution overlaid in grey for comparison. The broadband-excitation pulse spectra used for ultrafast experiments are in blue (resonant) and red (sub-resonant). Insets: absorbance spectra of **D1** and **D2** in CHX:Tol 3:1 (purple), Tol (green) and THF (orange), zoomed on the sub-gap absorption features. Equivalent insets for **D3**–**D5** are shown in Supplementary Fig. 7. CHX, cyclohexane; Tol, toluene; THF, tetrahydrofuran. Right: absorbance spectra for **M1**–**M5** prepared as thin films (black lines) are overlaid with the corresponding solution absorbance spectrum in grey. Wavelengths used for narrowband excitation are indicated by the blue (resonant) and red (sub-resonant) arrows. **c**, Orbital scheme for conventional SF compared to the coherent pathway presented in this Article. H and L denote highest occupied and lowest unoccupied molecular orbitals of interacting chromophores A and B involved in the SF process.

theoretical results[23–27]. This model has been invoked to explain reports of faint emission detected from ^{1}TT, which is typically likened to that of other dark states such as triplets, excimers and the $2A_g$ state in polyenes[24,28]. Despite this weak radiative pathway, direct S_0-to-^{1}TT excitation has never been observed. In this Article we revive the concept of a coherent SF pathway with a strikingly simple experimental approach of tuning the excitation energy. We demonstrate direct photoexcitation of dark ^{1}TT as a general phenomenon across a range of pentacene derivatives, indicating that photoexcitation of bright S_1 is no longer required to access the entangled pair.

Results

A library of pentacenes from strong to negligible coupling

The canonical system pentacene is known for its ability to rapidly and efficiently generate ^{1}TT after photoexcitation of S_1, so we utilized representative derivatives in the forms of covalent dimers (**D1**–**D5**) and monomeric thin films (**M1**–**M5**), as shown in Fig. 1a (Supplementary Section 1 provides synthesis and sample preparation details)[6,18]. Dimers **D1**–**D5** exhibit intramolecular SF and span the primary motifs studied so far: 6,6′-connected (**D1**–**D3**) versus 2,2′-connected (**D4**–**D5**), and joined with no linker (**D3**, **D4**), a small π-bridge (**D2**, **D5**) or a distinct chromophore (**D1**). SF in the 6,6′ structures is typically mediated by coupling of both S_1 and ^{1}TT to CT states, whereas the dynamics in 2,2′ structures depend on the weak, direct two-electron coupling between the S_1 and ^{1}TT states (Fig. 1c)[29–33]. Substantial shifts and splittings of the primary $S_0 \rightarrow S_1$ absorption bands in **D1** and **D2** compared to the monomer point to strong inter-pentacene couplings that result in a highly delocalized singlet state (Fig. 1b). By contrast, the negligible shift in **D4** and **D5** implies weak interactions leading to localized electronic character. Collectively, these characteristics result in intramolecular SF dynamics ranging from 0.7 ps to 200 ps in **D1**–**D5** (refs. 29–33). Previous studies have shown but overlooked a distinctive sub-gap absorption band (720–780 nm) in 6,6′ dimers (Supplementary Figs. 7 and 8)[31,32]. This feature is unrelated to aggregation (Supplementary Figs. 7 and 9), depends on the dielectric environment (Fig. 1b insets and Supplementary Figs. 7 and 10), and coincides with the expected energy of ^{1}TT, yet it is absent in the 2,2′ counterparts (Supplementary Figs. 7 and 8).

https://doi.org/10.1038/s41557-024-01556-3

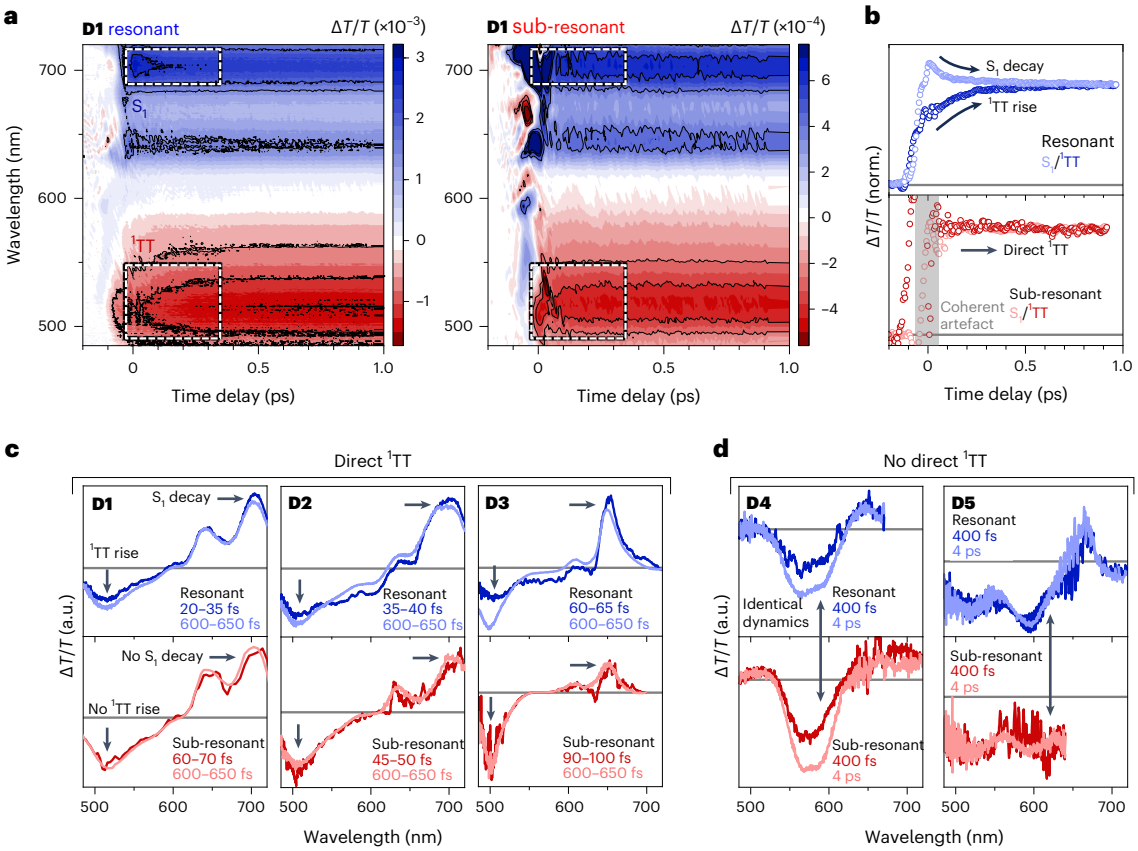

Fig. 2 | Ultrafast TA on D1–D5. a, Ultrafast TA contour maps of **D1** under resonant (left) and sub-resonant (right) excitation. White dashed boxes highlight the regions where S_1 decay (~705 nm) and ^{1}TT rise (~505 nm) are evident under resonant excitation, but absent under sub-resonant excitation. **b**, Normalized, integrated kinetic profiles of the S_1 (700–720 nm) and ^{1}TT (500–520 nm) signatures. The coherent artefact region is shaded grey. **c**, Spectra from TA contour maps of 6,6′ dimers integrated over the indicated time delays. Early and late spectra are presented for resonant (blue) and sub-resonant (red) photoexcitation, with the spectral positions of the signatures of $S_1 \rightarrow {}^1$TT conversion indicated by arrows, whether they are present or absent. The early-time spectra are extracted at the earliest resolvable time points beyond the coherent artefact, leading to slightly different accessible ranges in each molecule. **d**, Spectra from TA contour maps of 2,2′ dimers at the indicated time delays. Early and late spectra are presented for both resonant (blue) and sub-resonant (red) photoexcitation. All dimers were prepared as polystyrene matrices, which show nearly identical dynamics to solution measurements in CHX but exhibit minimal solvent and instrument artefacts. Extended Data Figs. 6–10 provide the full TA data.

Monomeric thin films **M1**–**M5** exhibit varying degrees of inter-pentacene coupling strengths—from strong to weak—as defined by the degree of spectral shift and distortion to the vibronic progression compared to isolated molecules in solution (Fig. 1b)[34]. The substantial spectral changes in thin films of **M2**–**M4** point to strong intermolecular coupling, whereas the more subtle spectral changes in **M1** are characteristic of moderate coupling[35]. The absorption of film **M5** is identical to the dilute solution, indicative of nearly negligible interactions. These coupling strengths generally align with the obtained single-crystal structures (Supplementary Section 4). Transient absorption (TA) measurements show that **M1**–**M5** all exhibit SF in the solid state (Extended Data Figs. 1–5 and Supplementary Fig. 12). The strong coupling between pentacene units in **M2** leads to sub-100-fs SF, attributed to a CT-mediated vibronic mechanism (Extended Data Fig. 2)[25,26]. The remaining strongly coupled films (**M3** and **M4**) exhibit comparably rapid SF (Extended Data Figs. 3 and 4), and, together with **M2**, these materials span H- to J-type coupling (Supplementary Fig. 11)[36]. Despite the weaker intermolecular coupling in **M1**, the SF rate is only slightly slower than in **M2**–**M4** (Extended Data Fig. 1). **M5** shows SF on a picosecond timescale due to the almost negligible inter-pentacene coupling in the ground state (Extended Data Fig. 5). In thin films, large linewidths and scattering tails prevent clear detection of equivalent sub-gap absorption bands to **D1**–**D2**.

Direct sub-resonant excitation of ^{1}TT in dimers

We probed the nature of the sub-gap absorption bands in **D1**–**D3** by monitoring the dynamics following photoexcitation with TA. In these experiments, positive signals stem from either bleaching of the ground state S_0 or stimulated emission from S_1, whereas negative signals originate from the absorption of excited states (S_1, ^{1}TT and so on). Together, these signals overlap to produce spectral and kinetic fingerprints of excited electronic states with time resolution limited by the duration of the excitation pulse. In our ultrafast TA measurements, we tailored two excitation pulses to be either resonant (520–680 nm, <10 fs) with the primary $S_0 \rightarrow S_1$ bands or sub-resonant (710–950 nm, <10 fs) to them (Supplementary Section 2 presents experimental details and Supplementary Fig. 6 the pulse characterization).

Ultrafast TA data for **D1** under resonant and sub-resonant excitation are presented in Fig. 2. Upon resonant excitation, we observed characteristic SF behaviour: a clear decay of the S_1 signature at 705 nm and a corresponding growth of the ^{1}TT signature at 505 nm (Fig. 2a, left, white dashed boxes). The S_0 and S_1 signatures overlap at the positive signal around 700 nm. Supplementary Fig. 13 shows a gradual shift in their relative contribution as the probe wavelength is scanned. Crucially, these dynamics are completely absent under sub-resonant excitation (Fig. 2a, right, white dashed boxes). Instead, the same ^{1}TT spectrum appears instantaneously upon sub-resonant excitation, and we observe no conversion dynamics in the sub-resonant kinetic

https://doi.org/10.1038/s41557-024-01556-3

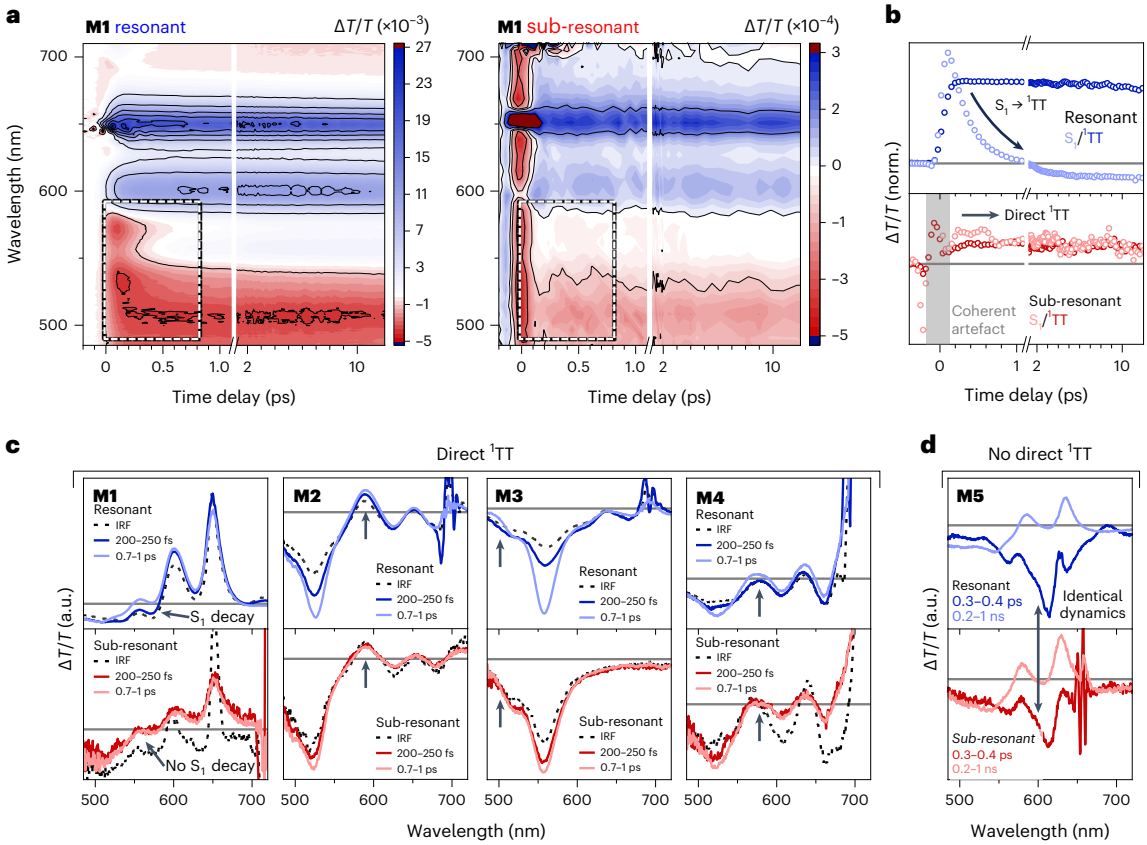

Fig. 3 | Narrowband TA on M1–M5. a, Narrowband TA contour maps of **M1** under resonant (left) and sub-resonant (right) excitation. White dashed boxes highlight the regions where S_1 decay (~550 nm) and ^{1}TT rise (~500 nm) are present under resonant excitation, but absent under sub-resonant excitation. **b**, Normalized, integrated kinetic profiles of the S_1 (530–580 nm) and ^{1}TT (480–505 nm) signatures. The coherent artefact region is indicated by a grey shaded region near time zero. **c**, Spectra from TA contour maps of strongly and moderately coupled films integrated over the indicated time delays. Early and late spectra are presented for resonant (blue) and sub-resonant (red) excitation, with the spectral position of the signatures of $S_1 \rightarrow {}^1$TT conversion indicated by arrows whether they are present or absent. The early-time spectra are extracted at the earliest resolvable time point beyond the instrument response. To maximize our sensitivity to short-lived S_1 signatures, we compare to the spectra collected during the instrument response (IRF; black dashed line). **d**, Spectra from TA contour maps of the weakly coupled **M5** at the indicated time delays. Early and late spectra are presented for both resonant (blue) and sub-resonant (red) photoexcitation. Extended Data Figs. 1–5 provide full TA data. Resonant and sub-resonant excitation wavelengths for each sample correspond to the red and blue arrows in Fig. 1 (**M1**, 650/700 nm; **M2**, 695/780 nm; **M3**, 690/775 nm; **M4**, 695/765 nm; **M5**, 625/660 nm).

profiles, despite our high temporal resolution (Fig. 2b). This result indicates that ^{1}TT is directly populated from the ground state, which is the central observation of this Article.

Extending the analysis to **D2**–**D5**, we observe the same general behaviour in 6,6′ dimers **D2** and **D3** (Fig. 2c). Under resonant excitation (top), there is a smooth transition from S_1 to ^{1}TT signatures, whereas sub-resonant excitation (bottom) leads to instantaneous ^{1}TT population. By contrast, the dynamics observed in the 2,2′ dimers are independent of excitation wavelength (Fig. 2d). We thus assign the weak, sub-gap absorption features in 6,6′ dimers **D1**–**D3** (Fig. 1b and Supplementary Figs. 7–10) to direct ^{1}TT absorption from the ground state. The 2,2′ dimers **D4** and **D5** lack this feature, and in those we do not observe direct ^{1}TT excitation. Comparing between **D2** and **D5** and between **D3** and **D4**, we infer that the defining characteristic for direct ^{1}TT generation is dimer connectivity rather than linker type. We return to this matter in the 'Discussion'.

Direct sub-resonant excitation of ^{1}TT in thin films

We observe the same direct ^{1}TT phenomenon in the intermolecular SF systems **M1**–**M4**, but it is absent in **M5**. In contrast to the dimers, we turn to narrowband TA to better distinguish between resonant and sub-resonant excitation conditions among the wider range of S_1 absorption energies in **M1**–**M5** (Extended Data Figs. 1–5 present measurements with ultrafast broadband pulses). Similarly to the measurements on dimers, we tuned our excitation pulses to be either resonant with the bright $S_0 \rightarrow S_1$ transition or sub-resonant, where the S_1 intensity has vanished (Fig. 1b, red and blue arrows; a more exhaustive excitation wavelength dependence is presented in Supplementary Figs. 14–19). Figure 3 shows the resonant and sub-resonant TA data for **M1**. Under resonant excitation, we resolve a clear conversion from S_1 to ^{1}TT signatures, similar to those in the 6,6′ dimers (Fig. 3a, left, white dashed box; Extended Data Fig. 1 provides an analysis of other spectral features). However, under sub-resonant excitation, there are no resolvable S_1 signatures—only instantaneously formed ^{1}TT signatures (Fig. 3a, right, white dashed box). Similarly, the sub-resonant kinetics in Fig. 3b show no sign of any state conversion. As in the 6,6′ dimers, this demonstrates direct ^{1}TT excitation from the ground state. We observe precisely the same phenomenon in all strongly coupled films, **M2**–**M4** (Fig. 3c and Extended Data Figs. 2–4), whereas the effect is absent in weakly coupled **M5** (Fig. 3d and Extended Data Fig. 5).

Absence of two-photon absorption and aggregate states

Although the multiexcitonic ^{1}TT state is formally dark, its direct absorption from the ground state could, in principle, occur through two-photon absorption. However, our observed linear excitation power dependence can rule out this mechanism, even under sub-resonant

https://doi.org/10.1038/s41557-024-01556-3

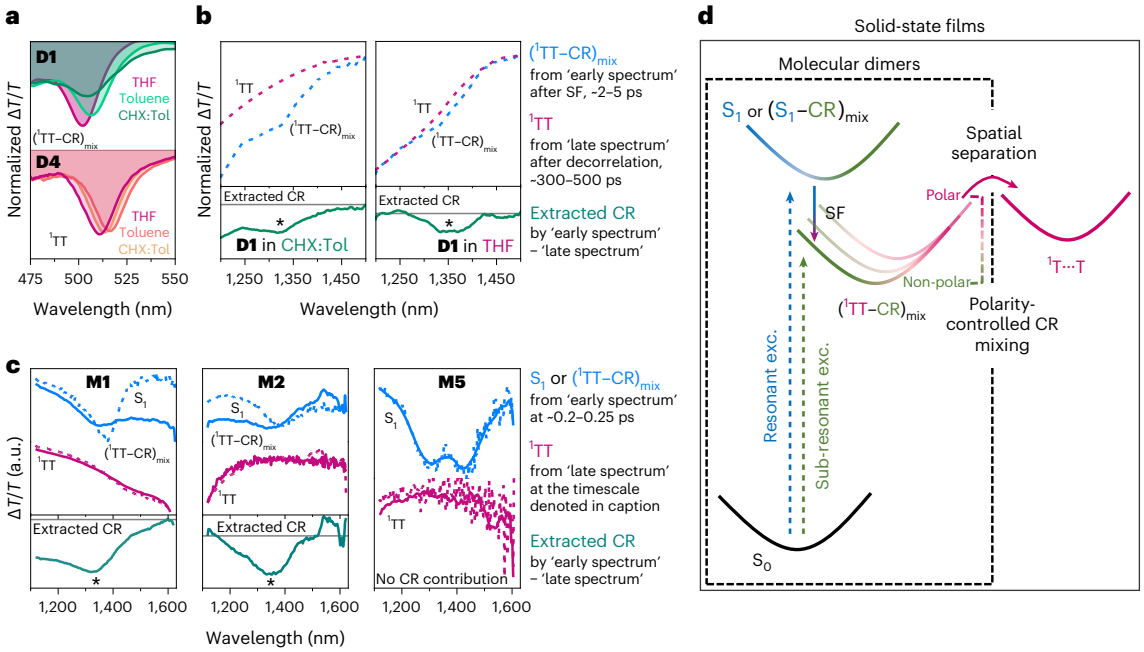

Fig. 4 | Charge resonance character in ^{1}TT. a, Solvent-dependent narrowband TA of **D1** and **D4** under resonant excitation (680 nm and 640 nm for **D1** and **D4**, respectively) in the visible range. Spectral slices were normalized to the ground-state bleach peak. Spectra were extracted by averaging for 1.5–2 ps, 2.5–3 ps and 3.5–4 ps for **D1** in CHX:Tol (3:1), Tol and THF, respectively. Spectra for **D4** were extracted by averaging from 10 to 20 ps. **b**, Narrowband TA for **D1** in the NIR range under resonant excitation in CHX:Tol (3:1) and THF. The blue dashed spectrum corresponds to the spectrum taken just after SF (1.5–2 ps for CHX:Tol and 3.5–4 ps for THF), and the red dashed spectrum corresponds to the spectrum after ^{1}TT decorrelation (300–500 ps). Spectra were normalized at 1,500 nm, and subtraction of the two produces the green spectra with extracted CR character. **c**, Narrowband TA spectral slices for **M1**, **M2** and **M5** in the NIR region. Solid and dotted spectra indicate sub-resonant and resonant excitation conditions. Blue spectra are the earliest resolvable spectral slices (200–250 fs), and red spectra are taken later after SF has occurred (20–100 ps for **M1** and **M2**, 200–1,000 ps for **M5**). The green spectra presented for **M1** and **M2** are obtained by subtracting the early/late spectra after normalization to extract the CR contribution to the ^{1}TT state. Asterisks indicate the expected CT band energy from the literature[30]. **d**, Scheme depicting CR character mixed into ^{1}TT, which enables its direct excitation from S_0.

excitation (Supplementary Figs. 20–22). Because dimers and monomeric films can be structurally disordered, it is also possible that a subset of aggregates or defect sites can undergo exceptionally rapid SF under sub-resonant excitation. These distinct populations would be evident in the S_0 ground-state bleach during a TA measurement, which is a fingerprint of what subset of molecules from the ensemble are excited. Moreover, a dynamic redshift of the bleach would be expected during migration to lower-energy sites. We see no systematic change to the ground-state bleach distribution to support the existence of such sites, in line with our absorption measurements (Fig. 1 and Supplementary Figs. 7–10). Additionally, a comparison of the TA lineshapes across our films or dimers indicates that the ^{1}TT spectral fingerprint varies strongly with the inter-pentacene coupling. We would thus expect unique aggregate or defect sites to similarly exhibit distinguishable ^{1}TT spectral signatures, but we detect, identically, the same ^{1}TT fingerprint, regardless of excitation wavelength. Finally, the results in Fig. 3 are further corroborated by systematically tuning the excitation wavelength (Supplementary Figs. 14–19). In **D4**, **D5** and **M5**, which do not undergo direct ^{1}TT, we find identical SF dynamics, regardless of photoexcitation condition, ruling out distinct sub-gab S_1 states with different SF rates.

Based on our steady-state and TA measurements, it is evident that ^{1}TT can be directly photoexcited by pumping below the optical bandgap in a wide range of pentacene materials. Importantly, however, the effect varies from system to system, pointing to underlying design principles, which we address in the 'Discussion'. Regardless of how ^{1}TT is generated, either directly or through S_1, its subsequent evolution, decoherence and decay are all the same in monomeric films (Supplementary Figs. 23 and 24); that is, the same spin-entangled ^{1}TT state is generated under direct photoexcitation without the need to start in S_1. This direct ^{1}TT excitation in both dimers and thin films is also a rare instance where the same mechanistic phenomenon can be observed in intra- and intermolecular SF systems, despite the very different interactions that drive them.

Discussion

The direct excitation of ^{1}TT from the ground state is contrary to the conventional understanding of this state, where it is exclusively formed via SF from bright S_1 or the annihilation of independent triplets[6,18,37,38]. Instead, our observations recall the widely debated proposals of 'coherent' SF, whereby ^{1}TT is directly photoexcited via quantum superposition with S_1. Here we propose that the origin of direct ^{1}TT excitation is coherent mixing between ^{1}TT and a charge resonance (CR) state. As described in Fig. 1c, ^{1}TT is developed from the ground state through the exchange of two electrons between pentacene units, by one-electron transfer integrals (J) from highest occupied molecular orbital A (H_A) to lowest unoccupied molecular orbital B (L_B) and vice versa. This state thus shares symmetry with the CR state, a symmetric superposition of one-electron CT states, and accordingly they mix through a first-order perturbation via J (Fig. 1c). The resulting mixed state should likewise be dark, as CR is not typically a bright state, but it carries finite transition probability borrowed from the main excitonic transition ($S_0 \rightarrow S_1$), which enables the coherent photoexcitation of ^{1}TT[39]. This mechanism provides a rationale for the observed link between the ability to directly excite ^{1}TT and the spectral signatures of inter-pentacene coupling identified in Fig. 1b. The delocalized frontier molecular orbitals associated with such coupling often incorporate intermolecular CT character in asymmetric systems or CR character in symmetric systems[39–41]. Electronic delocalization is potentially a crucial factor in increasing J and thereby the optical accessibility of ^{1}TT.

We can directly evaluate the impact of CR mixing in dimers by controlling the solvent dielectric constant (Fig. 4a and Supplementary Figs. 25–39). Following SF in 6,6′ dimers in polar media like tetrahydrofuran (THF), we detect the prototypical sharp fingerprint of ^{1}TT excited-state absorption. As we shift towards nonpolar media like cyclohexane (CHX), the ^{1}TT peak broadens and weakens in molar extinction (Fig. 4a, top). These changes are accompanied by the increased prominence of a narrow excited-state absorption at 1,350 nm (Supplementary Fig. 25). These effects are hallmarks of increased mixing with CR[30]. The counterintuitive increase in CR mixing with a decrease in polarity is a consequence of symmetry; only in nonpolar media does the CR remain a fully symmetric superposition, able to mix effectively with ^{1}TT. Symmetry-breaking through solvent–solute interactions suppresses this mixing and leads to excitations with a more localized character. In the 2,2′ structures, we observe none of these effects (Fig. 4a, bottom). The ^{1}TT lineshape remains consistent over the full solvent range, and we find no evidence for CR mixing. We can rationalize the manifestations of CR character in our experiments with existing theoretical and experimental understanding of pentacene dimers. In the 2,2′ structures, S_1 and ^{1}TT are nearly pure electronic states[42–44], and their interaction arises through weak direct S_1–^{1}TT coupling or a super-exchange mechanism mediated by a high-energy CT state (400–500 nm)[6,45]. In some cases, this state becomes bright enough to appear in steady-state absorption through mixing with a higher-lying Frenkel excitonic state[44,46,47]. Nevertheless, these interactions are too weak to substantially modify the character of S_1 and ^{1}TT, and ^{1}TT remains dark. In 6,6′ structures, the symmetric superposition of CTs, CR, directly interacts with S_1 and ^{1}TT to form mixed states. This CR mixing regime is highly sensitive to the dielectric environment, as CR separates into a higher- and lower-energy pair of asymmetric CT states in polar medium[31,43]. Only in nonpolar media, where CR character is strongly mixed into S_1 and ^{1}TT, do the 6,6′ structures permit direct ^{1}TT excitation. For a more detailed discussion on the role of chromophore connectivity (2,2′ versus 6,6′) in CR mixing, we direct readers to refs. 31,42–47.

Understanding these signatures, we can directly resolve the contribution of CR character through analysis of the TA spectra in the near-infrared (Fig. 4b–c and Supplementary Fig. 40). Immediately after SF has occurred in dimers, the resulting ^{1}TT spectrum possesses a sharp peak superimposed near 1,350 nm, which diminishes during ^{1}TT decorrelation (Fig. 4b). On long timescales after SF in thin films, the spectra following resonant and sub-resonant excitation precisely match for all samples, highlighting that we achieve the same triplet states regardless of excitation pathway (Fig. 4c, red, and Supplementary Fig. 24). The early-time spectra following resonant excitation naturally contain the unique hallmarks of S_1 as the primary photoexcitation (Fig. 4c, blue dashed line). Intriguingly, the spectrum of the initial state after sub-resonant excitation is ^{1}TT-like but carries a clear additional band (Fig. 4c, blue solid line). Our analysis in Figs. 2 and 3 rules out that this species is related to S_1, and simple spectral subtraction ('early' − 'late') reveals a distinct peak at ~1,350 nm that is instead characteristic of CR[30]. As seen earlier, this feature is present whenever ^{1}TT is directly excited, but absent in **D4**, **D5** and **M5** where the primary photoexcitation remains S_1. We thus find that direct excitation of ^{1}TT is correlated with ^{1}TT–CR mixing across our materials library, although the subsequent fate of this mixed state depends on the accessibility of a triplet separation pathway (Fig. 4d). For example, in the solid state, triplet hopping from ^{1}TT can result in the less-coupled pair state ^{1}T…T. The key signature of this phenomenon is a delayed growth in the apparent triplet signature in TA, well after S_1 is fully depleted or, as reported here, even when S_1 is never populated in the first place (Figs. 3c,d and 4b and Supplementary Fig. 41)[48–50]. Our model provides essential insight into this behaviour. Within the coherently mixed ^{1}TT–CR state, the extinction is spread across both localized triplet-based (visible) and delocalized CR-based near-infrared (NIR) transitions. As hopping leads to localized triplet states, the optical spectra are reweighted away from the delocalized CR transitions. The resulting photoinduced absorption growth dynamics thus reports on a change in the nature of the excitation, rather than a change in populations.

Conclusion

Our method of direct excitation of ^{1}TT provides essential insights into the mechanism of SF following the coherent ^{1}TT–CR pathway and even in the conventional pathway beginning in bright S_1. The fingerprints of CR-mediated coupling in the solid state have been elusive since the inception of the field, and only very challenging orbital-resolved photoelectron spectroscopy has been able to capture these signatures, in just one material system[19]. Our simple approach comparing coherent ^{1}TT–CR with subsequent ^{1}TT yields the most direct optical signatures of the CR contribution, and we find that these features are present across many materials, regardless of the initial photoexcited state. Indeed, we expect the same approach will shed light on other photophysical pathways where mixed dark states are implicated, such as thermally activated delayed fluorescence. Extension of our method with more detailed wavelength scanning should afford a powerful tool to determine the vertical energy of ^{1}TT and its binding energy relative to free triplets—important design parameters that are generally unknown. More broadly, our observation demonstrates that multiple distinct SF pathways can be active in the same material—incoherent via S_1, and direct excitation—and the balance between them can be tuned by the excitation wavelength. Factoring in the vibronic structure of ^{1}TT (Fig. 1b, insets), even in the resonant excitation condition we expect a small contribution from the coherent pathway, but this contribution has previously been overlooked[11,22,23]. In principle, this pathway permits direct generation of entangled triplet pairs for solar cell applications or quantum information science, but the effect is limited by the low extinction of ^{1}TT in the pentacenes studied here[14–18]. Crucially, our results show that this phenomenon is not universal but material-dependent and thus optimizable. In some cases, the CR mixing is strong enough for the transition to appear even in the steady state. Tuning the state mixing between ^{1}TT and CR, which is closely linked to electronic delocalization, holds promise as a new design principle to maximize the benefits of coherent photoexcitation of ^{1}TT.

Online content

Any methods, additional references, Nature Portfolio reporting summaries, source data, extended data, supplementary information, acknowledgements, peer review information; details of author contributions and competing interests; and statements of data and code availability are available at https://doi.org/10.1038/s41557-024-01556-3.

References

1. Schloemer, T. et al. Nanoengineering triplet–triplet annihilation upconversion: from materials to real-world applications. *ACS Nano* **17**, 3259–3288 (2023).
2. Carrod, J. A., Gray, V. & Börjesson, K. Recent advances in triplet-triplet annihilation upconversion and singlet fission, towards solar energy applications. *Energy Environ. Sci.* **15**, 4982–5016 (2022).
3. Cowan, A. J. & Durrant, J. R. Long-lived charge separated states in nanostructured semiconductor photoelectrodes for the production of solar fuels. *Chem. Soc. Rev.* **42**, 2281–2293 (2013).
4. Coropceanu, V., Chen, X.-K., Wang, T., Zheng, Z. & Brédas, J.-L. Charge-transfer electronic states in organic solar cells. *Nat. Rev. Mater.* **4**, 689–707 (2019).
5. Köhler, A. & Bässler, H. *Electronic Processes in Organic Semiconductors* (Wiley, 2015); https://doi.org/10.1002/9783527685172
6. Smith, M. B. & Michl, J. Singlet fission. *Chem. Rev.* **110**, 6891–6936 (2010).

7. Monahan, N. & Zhu, X.-Y. Charge transfer-mediated singlet fission. *Annu. Rev. Phys. Chem.* **66**, 601–618 (2015).
8. Casillas, R. et al. Molecular insights and concepts to engineer singlet fission energy conversion devices. *Energy Environ. Sci.* **13**, 2741–2804 (2020).
9. Le, A. K. et al. Singlet fission involves an interplay between energetic driving force and electronic coupling in perylenediimide films. *J. Am. Chem. Soc.* **140**, 814–826 (2018).
10. Miyata, K., Conrad-Burton, F. S., Geyer, F. L. & Zhu, X.-Y. Triplet pair states in singlet fission. *Chem. Rev.* **119**, 4261–4292 (2019).
11. Musser, A. J. & Clark, J. Triplet-pair states in organic semiconductors. *Annu. Rev. Phys. Chem.* **70**, 323–351 (2019).
12. Sanders, S. N. et al. Understanding the bound triplet-pair state in singlet fission. *Chem* **5**, 1988–2005 (2019).
13. Piland, G. B., Burdett, J. J., Dillon, R. J. & Bardeen, C. J. Singlet fission: from coherences to kinetics. *J. Phys. Chem. Lett.* **5**, 2312–2319 (2014).
14. Smyser, K. E. & Eaves, J. D. Singlet fission for quantum information and quantum computing: the parallel JDE model. *Sci. Rep.* **10**, 18480 (2020).
15. Wasielewski, M. R. et al. Exploiting chemistry and molecular systems for quantum information science. *Nat. Rev. Chem.* **4**, 490–504 (2020).
16. Lee, J. et al. Singlet exciton fission photovoltaics. *Acc. Chem. Res.* **46**, 1300–1311 (2013).
17. Einzinger, M. et al. Sensitization of silicon by singlet exciton fission in tetracene. *Nature* **571**, 90–94 (2019).
18. Wilson, M. W. B., Rao, A., Ehrler, B. & Friend, R. H. Singlet exciton fission in polycrystalline pentacene: from photophysics toward devices. *Acc. Chem. Res.* **46**, 1330–1338 (2013).
19. Neef, A. et al. Orbital-resolved observation of singlet fission. *Nature* **616**, 275–279 (2023).
20. Chan, W.-L. et al. Observing the multiexciton state in singlet fission and ensuing ultrafast multielectron transfer. *Science* **334**, 1541–1545 (2011).
21. Musser, A. J. et al. Evidence for conical intersection dynamics mediating ultrafast singlet exciton fission. *Nat. Phys.* **11**, 352–357 (2015).
22. Schnedermann, C. et al. A molecular movie of ultrafast singlet fission. *Nat. Commun.* **10**, 4207 (2019).
23. Bakulin, A. A. et al. Real-time observation of multiexcitonic states in ultrafast singlet fission using coherent 2D electronic spectroscopy. *Nat. Chem.* **8**, 16–23 (2016).
24. Yong, C. K. et al. The entangled triplet pair state in acene and heteroacene materials. *Nat. Commun.* **8**, 15953 (2017).
25. Beljonne, D., Yamagata, H., Brédas, J. L., Spano, F. C. & Olivier, Y. Charge-transfer excitations steer the Davydov splitting and mediate singlet exciton fission in pentacene. *Phys. Rev. Lett.* **110**, 226402 (2013).
26. Yost, S. R. et al. A transferable model for singlet-fission kinetics. *Nat. Chem.* **6**, 492–497 (2014).
27. Berkelbach, T. C., Hybertsen, M. S. & Reichman, D. R. Microscopic theory of singlet exciton fission. I. General formulation. *J. Chem. Phys.* **138**, 114102 (2013).
28. Polívka, T. & Sundström, V. Ultrafast dynamics of carotenoid excited states—from solution to natural and artificial systems. *Chem. Rev.* **104**, 2021–2072 (2004).
29. Sanders, S. N. et al. Quantitative intramolecular singlet fission in bipentacenes. *J. Am. Chem. Soc.* **137**, 8965–8972 (2015).
30. Lukman, S. et al. Tuning the role of charge-transfer states in intramolecular singlet exciton fission through side-group engineering. *Nat. Commun.* **7**, 13622 (2016).
31. Krishnapriya, K. C. et al. Spin density encodes intramolecular singlet exciton fission in pentacene dimers. *Nat. Commun.* **10**, 33 (2019).
32. Zirzlmeier, J. et al. Singlet fission in pentacene dimers. *Proc. Natl Acad. Sci. USA* **112**, 5325–5330 (2015).
33. Ringström, R. et al. Molecular rotational conformation controls the rate of singlet fission and triplet decay in pentacene dimers. *Chem. Sci.* **13**, 4944–4954 (2022).
34. Pensack, R. D. et al. Striking the right balance of intermolecular coupling for high-efficiency singlet fission. *Chem. Sci.* **9**, 6240–6259 (2018).
35. Tayebjee, M. J. Y. et al. Morphological evolution and singlet fission in aqueous suspensions of TIPS-pentacene nanoparticles. *J. Phys. Chem. C* **120**, 157–165 (2016).
36. Hestand, N. J. & Spano, F. C. Molecular aggregate photophysics beyond the Kasha Model: novel design principles for organic materials. *Acc. Chem. Res.* **50**, 341–350 (2017).
37. Casanova, D. Theoretical modeling of singlet fission. *Chem. Rev.* **118**, 7164–7207 (2018).
38. Kim, H. & Zimmerman, M. P. Coupled double triplet state in singlet fission. *Phys. Chem. Chem. Phys.* **20**, 30083–30094 (2018).
39. Aryanpour, K., Shukla, A. & Mazumdar, S. Theory of singlet fission in polyenes, acene crystals, and covalently linked acene dimers. *J. Phys. Chem. C* **119**, 6966–6979 (2015).
40. Yamagata, H. et al. The nature of singlet excitons in oligoacene molecular crystals. *J. Chem. Phys.* **134**, 204703 (2011).
41. Cudazzo, P., Gatti, M. & Rubio, A. Excitons in molecular crystals from first-principles many-body perturbation theory: picene versus pentacene. *Phys. Rev. B* **86**, 195307 (2012).
42. Khan, S. & Mazumdar, S. Diagrammatic exciton basis theory of the photophysics of pentacene dimers. *J. Phys. Chem. Lett.* **8**, 4468–4478 (2017).
43. Korovina, N. V., Pompetti, N. F. & Johnson, J. C. Lessons from intramolecular singlet fission with covalently bound chromophores. *J. Chem. Phys.* **152**, 040904 (2020).
44. Parenti, K. R. et al. Quantum interference effects elucidate triplet-pair formation dynamics in intramolecular singlet-fission molecules. *Nat. Chem.* **15**, 339–346 (2023).
45. Fuemmeler, E. G. et al. A direct mechanism of ultrafast intramolecular singlet fission in pentacene dimers. *ACS Cent. Sci.* **2**, 316–324 (2016).
46. Hele, T. J. H. et al. Anticipating acene-based chromophore spectra with molecular orbital arguments. *J. Phys. Chem. A* **123**, 2527–2536 (2019).
47. Kobayashi, Y. & Leone, S. R. Characterizing coherences in chemical dynamics with attosecond time-resolved X-ray absorption spectroscopy. *J. Chem. Phys.* **157**, 180901 (2022).
48. Lee, T. S. et al. Triplet energy transfer governs the dissociation of the correlated triplet pair in exothermic singlet fission. *J. Phys. Chem. Lett.* **9**, 4087–4095 (2018).
49. Munson, K. T. et al. Ultrafast triplet pair separation and triplet trapping following singlet fission in amorphous pentacene films. *J. Phys. Chem. C* **124**, 23567–23578 (2020).
50. Korovina, N. V., Chang, C. H. & Johnson, J. C. Spatial separation of triplet excitons drives endothermic singlet fission. *Nat. Chem.* **12**, 391–398 (2020).

Methods

Synthesis

Preparation of the pentacene systems (**D1**–**D5** and **M1**–**M5**) is described in detail in Supplementary Section 1.

Steady-state spectroscopy

Steady-state absorption spectra were collected using a Cary 5000 UV–vis–NIR spectrometer or a simple home-built set-up using a white-light source (LDLS EQ-99X, Energetiq) and a spectrometer (AvaSpec-Mini4096CL, Avantes).

Time-resolved spectroscopy

Narrowband and broadband TA measurements were carried out using a Yb:KGW regenerative amplifier system (Pharos, Light Conversion). Narrowband TA measurements were performed using a commercial Helios TA spectrometer (Ultrafast Systems) with a collinear optical parametric amplifier (Orpheus, Light Conversion). Broadband sub-10-fs TA measurements were performed using two separate home-built noncollinear optical parametric amplifiers (NOPAs) in the visible (520–680 nm) and NIR (700–900 nm) energy regions. Detailed descriptions are provided in Supplementary Section 2.

Data availability

The online version of this paper includes Supplementary Information, including synthetic and experimental details, figures and text. All data are available from the corresponding authors upon reasonable request. Crystallographic data for the structures reported in this article have been deposited at the Cambridge Crystallographic Data Centre, under deposition nos. CCDC 2353076 (**M1**), 722606 (**M3**) and 2353077 (**M4**). Copies of the data can be obtained free of charge via https://www.ccdc.cam.ac.uk/structures/. Source data are provided with this paper.

Acknowledgements

This work made use of the Cornell Center for Materials Research Shared Facilities, which are supported through the NSF MRSEC programme (DMR-1719875). This work was supported by the College of Arts and Sciences at Cornell University (A.J.M.), the US Department of Energy, Office of Science, Basic Energy Sciences, Condensed Phase and Interfacial Molecular Science, Early Career Research Program DE-SC0021941 (A.J.M.), the Alfred P. Sloan Foundation (A.J.M.), Cornell Atkinson Center for Sustainability (A.J.M.), the National Research Foundation of Korea funded by the Ministry of Education 2022R1A6A3A03072477 (J.K.), a National Research Foundation of Korea Grant funded by the Korean Government RS-2023-00210400 (W.K.), National Science Foundation grant no. DMR-1627428 (J.A.), and the Science and Engineering Research Board (SERB), India, through IRHPA grant IPA/2020/000033 and core research grant CRG/2022/004523 (S.P.).

Author contributions

A.J.M. and W.K. conceived the project. K.M., D.W., J.F., J.W., S.P. and J.A. synthesized the samples and D.C.B. and V.D. prepared thin films using these materials. J.K. and D.C.B. designed the experiments and performed the narrowband and broadband TA measurements. J.K., D.C.B., W.K. and A.J.M. led the analysis of the datasets and wrote the paper with input from all authors. All authors contributed to discussions.

Competing interests

The authors declare no competing interests.

Additional information

Extended data is available for this paper at https://doi.org/10.1038/s41557-024-01556-3.

Supplementary information The online version contains supplementary material available at https://doi.org/10.1038/s41557-024-01556-3.

Correspondence and requests for materials should be addressed to Woojae Kim or Andrew J. Musser.

Peer review information *Nature Chemistry* thanks the anonymous reviewers for their contribution to the peer review of this work.

https://doi.org/10.1038/s41557-024-01556-3

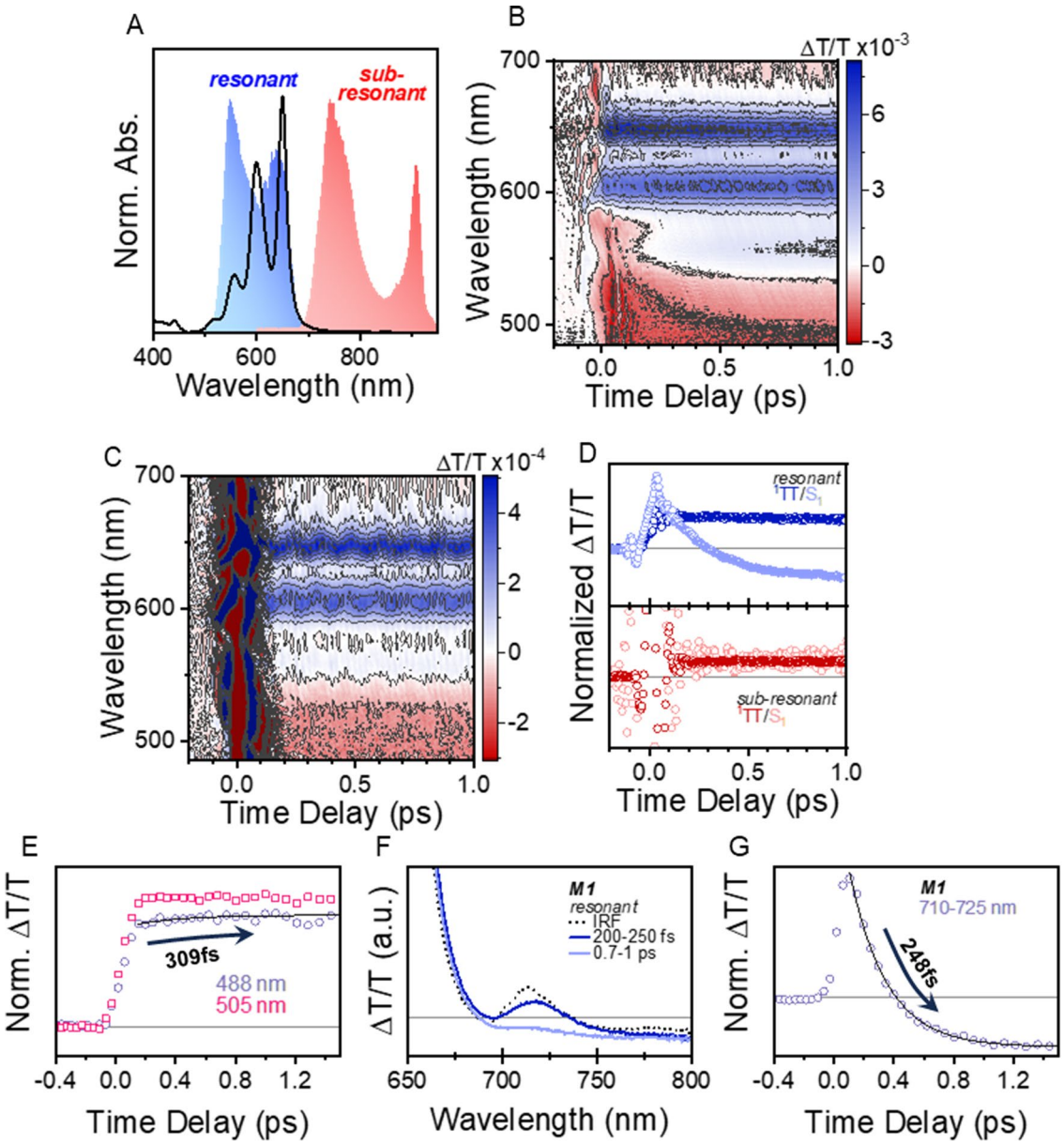

Extended Data Fig. 1 | TA of film M1. (**a**) Absorbance spectrum of **M1** compared to the ultrafast resonant and sub-resonant excitation pulses. Broadband ultrafast TA data for **M1** using resonant (**b**) and sub-resonant **(c)** excitation pulses along with comparison of respective kinetics **(d)**. Results show direct ^{1}TT excitation under sub-resonant excitation in agreement with the narrowband TA presented in Fig. 3. Kinetics in **D** were extracted by integrating from 480–505 nm for ^{1}TT and 530–580 nm for S_1. **(e)** `^{1}TT kinetic extracted at single wavelengths rather than by integration as done in Fig. 3b. The kinetic trace extracted at 488 nm shows a rise with similar time constant to the S_1 decay in Fig. 3b (309 vs. 260 fs), whereas a kinetic extracted where there is more spectral overlap with S_1 shows nearly no rise. (**f** and **g**) `TA spectra for **M1** zoomed on the stimulated emission peak along with its respective kinetic showing similar time constant (248 fs) to the above ^{1}TT rise and corresponding ^{1}TT decay from main text.

https://doi.org/10.1038/s41557-024-01556-3

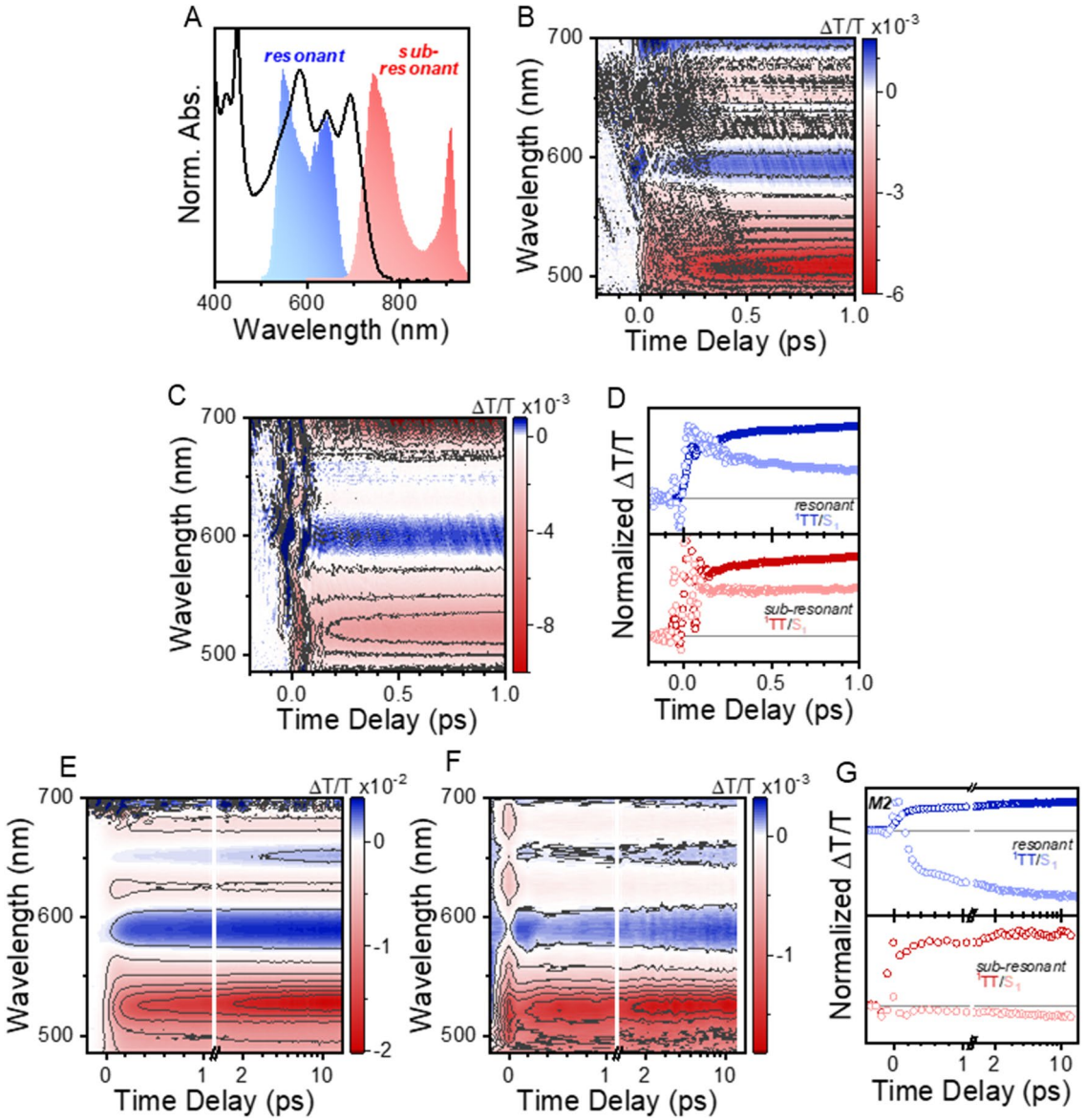

Extended Data Fig. 2 | TA of film M2. (a) Absorbance spectrum of **M2** compared to the ultrafast resonant and sub-resonant excitation pulses. The absorbance spectrum of **M2** has too much overlap with the sub-resonant excitation pulse to selectively excite just ^{1}TT. Broadband ultrafast TA data for **M2** using resonant **(b)** and sub-resonant **(c)** excitation pulses along with comparison of respective kinetics **(d)**. Full narrowband TA data under resonant **(e)** and sub-resonant **(f)** excitation for **M2** for which spectral slices are presented in Fig. 3 along with comparison of respective kinetics **(g)**. Kinetics in **D** and **G** were extracted by integrating from 515–540 nm for ^{1}TT and 560–620 nm for S_1.

https://doi.org/10.1038/s41557-024-01556-3

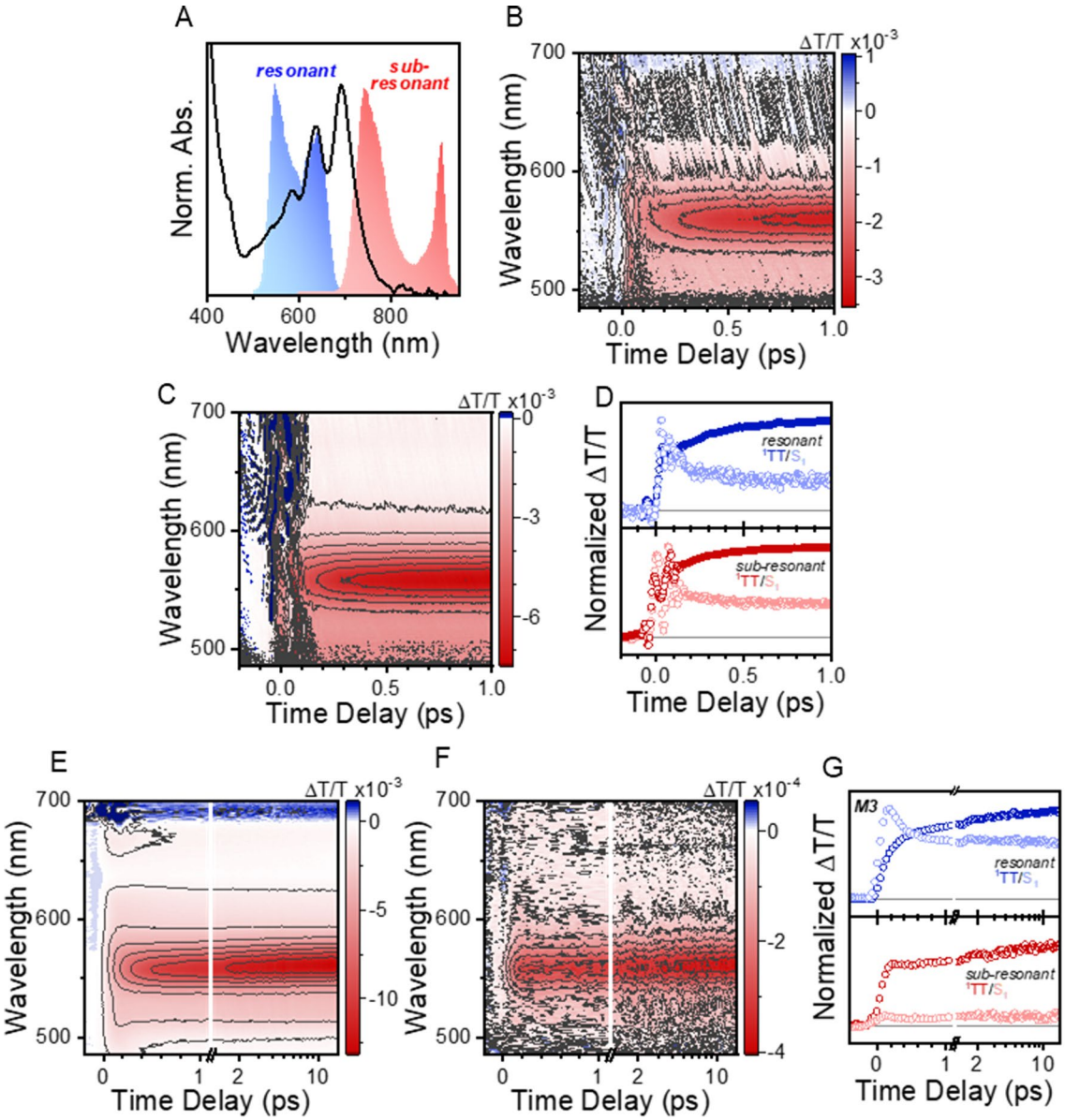

Extended Data Fig. 3 | TA of film M3. (a) Absorbance spectrum of **M3** compared to the ultrafast resonant and sub-resonant excitation pulses. The absorbance spectrum of **M3** has too much overlap with the sub-resonant excitation pulse to selectively excite just ^{1}TT. Broadband ultrafast TA data for **M3** using resonant **(b)** and sub-resonant **(c)** excitation pulses along with comparison of respective kinetics **(d)**. Full narrowband TA data under resonant **(e)** and sub-resonant **(f)** excitation for **M3** for which spectral slices are presented in Fig. 3 along with comparison of respective kinetics **(g)**. Kinetics in **D** and **G** were extracted by integrating from 550–580 nm for ^{1}TT and 480–520 nm for S_1.

https://doi.org/10.1038/s41557-024-01556-3

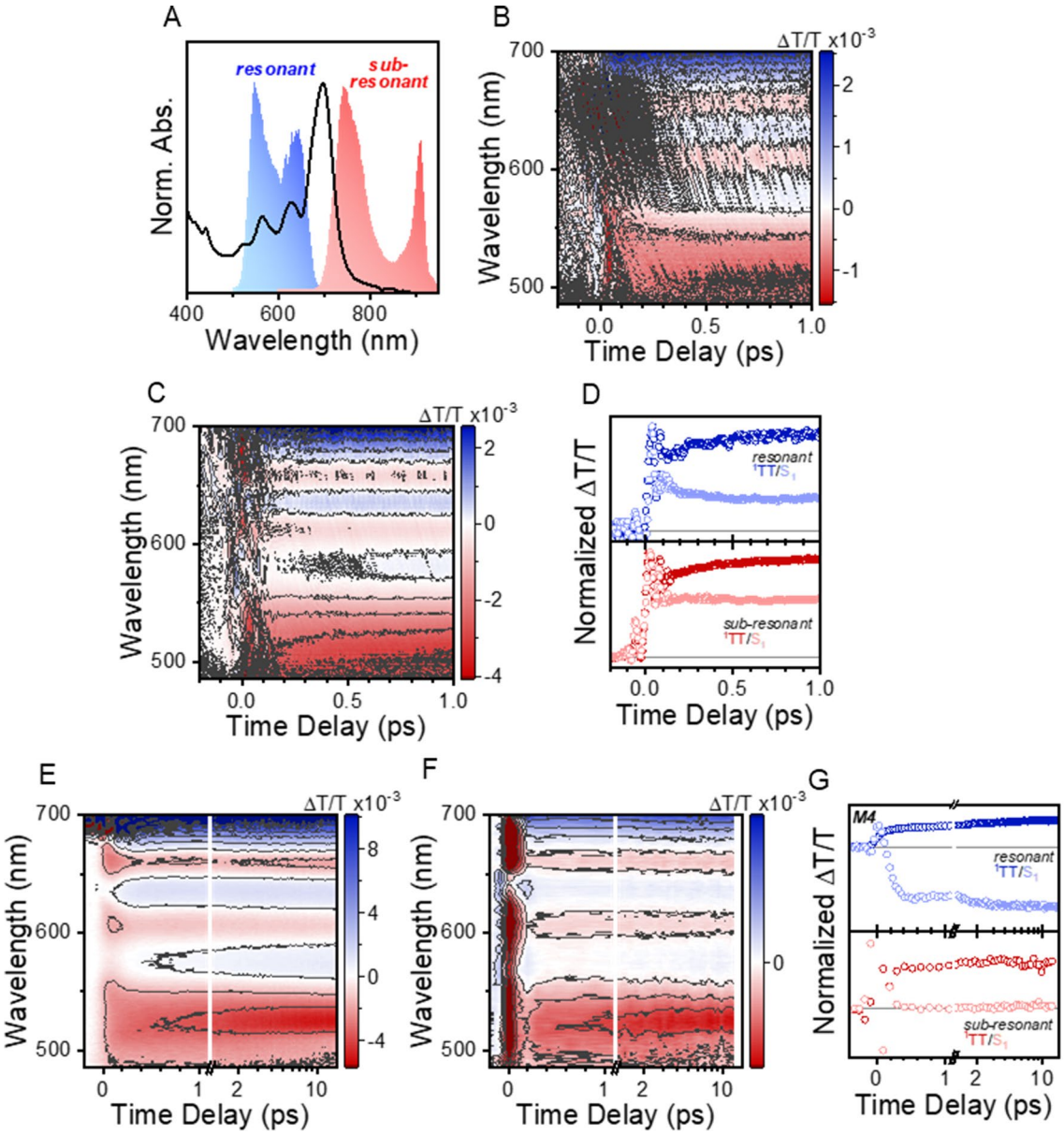

Extended Data Fig. 4 | TA of film M4. (**a**) Absorbance spectrum of **M4** compared to the ultrafast resonant and sub-resonant excitation pulses. The absorbance spectrum of **M4** has too much overlap with the sub-resonant excitation pulse to selectively excite just ^{1}TT. Broadband ultrafast TA data for **M4** using resonant (**b**) and sub-resonant (**c**) excitation pulses along with comparison of respective kinetics (**d**). Full narrowband TA data under resonant (**e**) and sub-resonant (**f**) excitation for **M4** for which spectral slices are presented in Fig. 3 along with comparison of respective kinetics (**g**). Kinetics in **D** and **G** were extracted by integrating from 520–540 nm for ^{1}TT and 620–640 nm for S_1.

https://doi.org/10.1038/s41557-024-01556-3

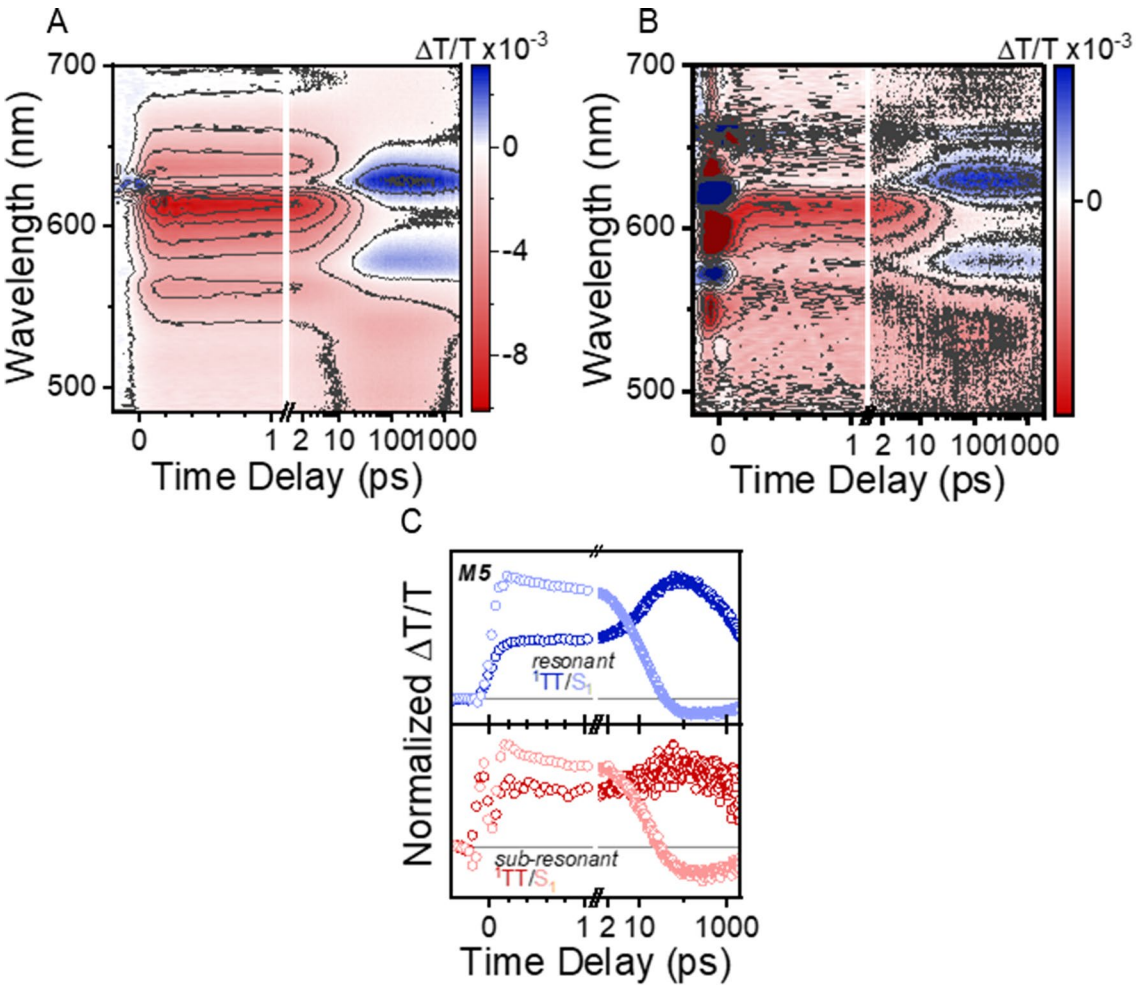

Extended Data Fig. 5 | TA of film M5. Full narrowband TA data under resonant (**a**) and sub-resonant (**b**) excitation for **M5** for which spectral slices are presented in Fig. 3 along with comparison of respective kinetics (**c**). There is no evidence for direct ^{1}TT excitation in this sample. Kinetics in **C** were extracted by integrating from 480–520 nm for ^{1}TT and 560–660 nm for S_1.

https://doi.org/10.1038/s41557-024-01556-3

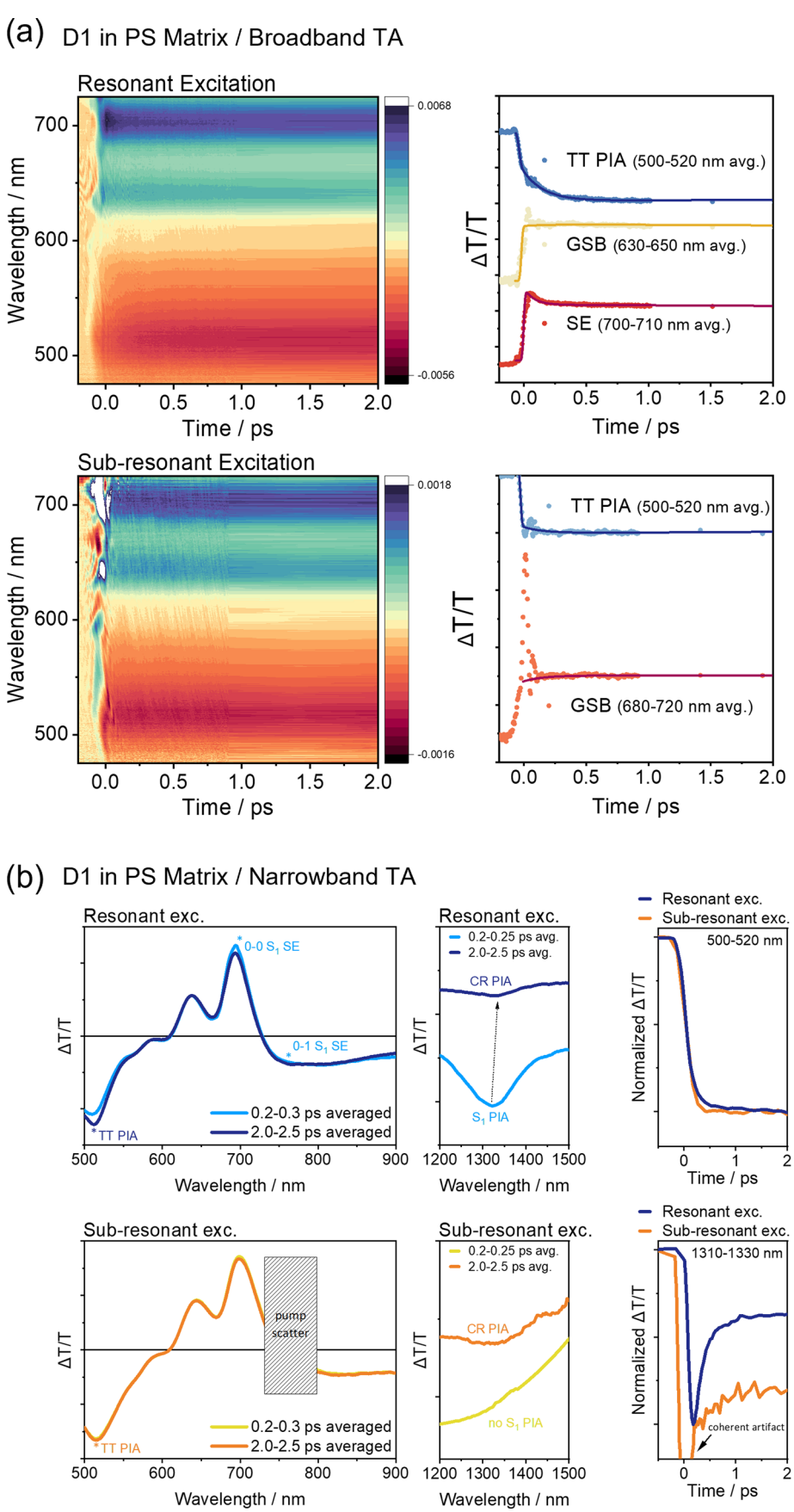

Extended Data Fig. 6 | TA of dimer D1. (a) Broadband ultrafast TA measurements on **D1** in polystyrene matrix. 2D contour maps (left) and temporal profiles (right) are plotted. **(b)** Narrowband TA measurements on **D1** in polystyrene matrix. Representative TA spectra in visible region (left) & near-infrared region (middle) and decay profiles (right) are plotted.

https://doi.org/10.1038/s41557-024-01556-3

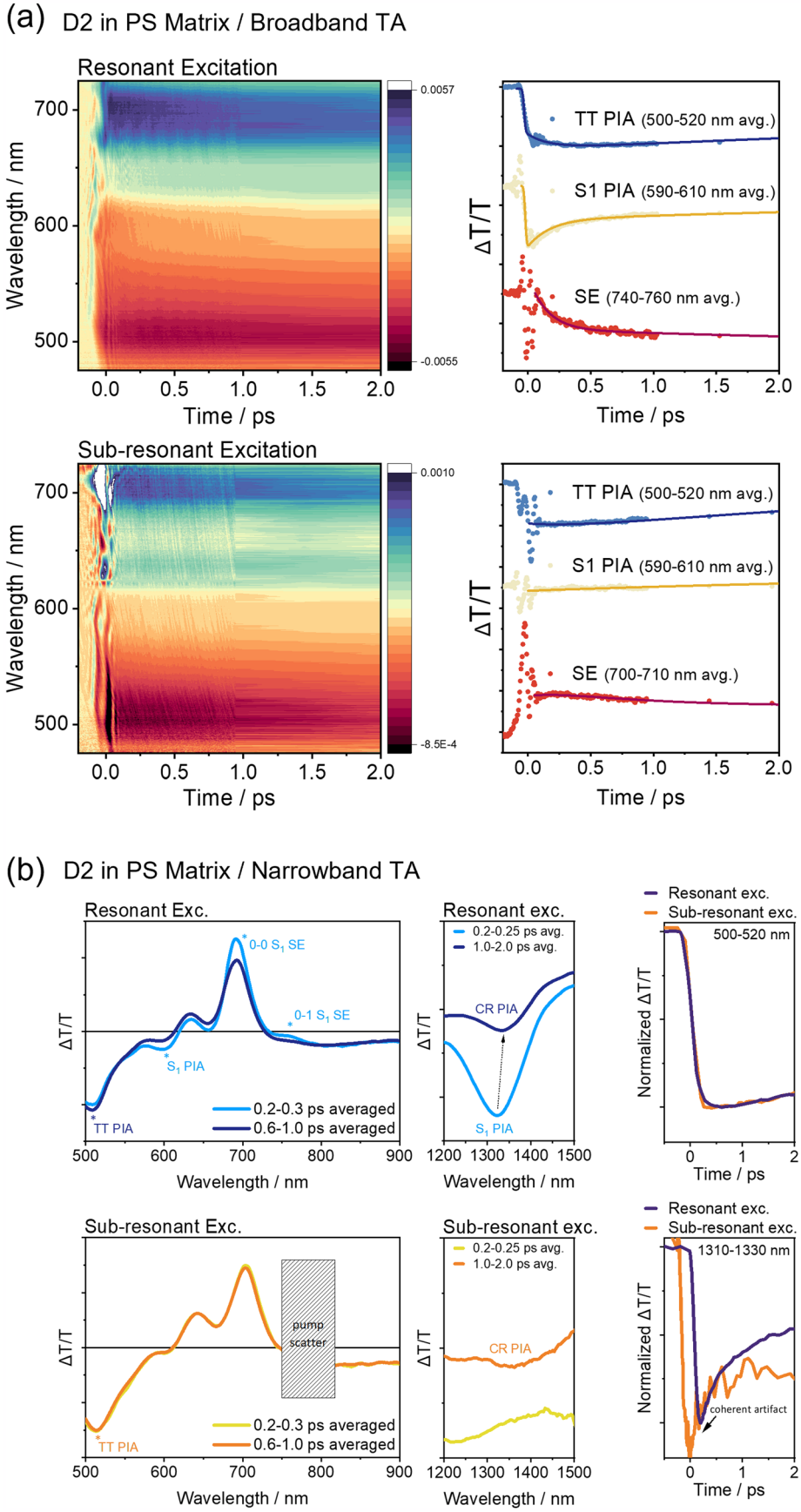

Extended Data Fig. 7 | TA of dimer D2. (a) Broadband ultrafast TA measurements on **D2** in polystyrene matrix. 2D contour maps (left) and temporal profiles (right) are plotted. **(b)** Narrowband TA measurements on **D2** in polystyrene matrix. Representative TA spectra in visible region (left) & near-infrared region (middle) and decay profiles (right) are plotted.

https://doi.org/10.1038/s41557-024-01556-3

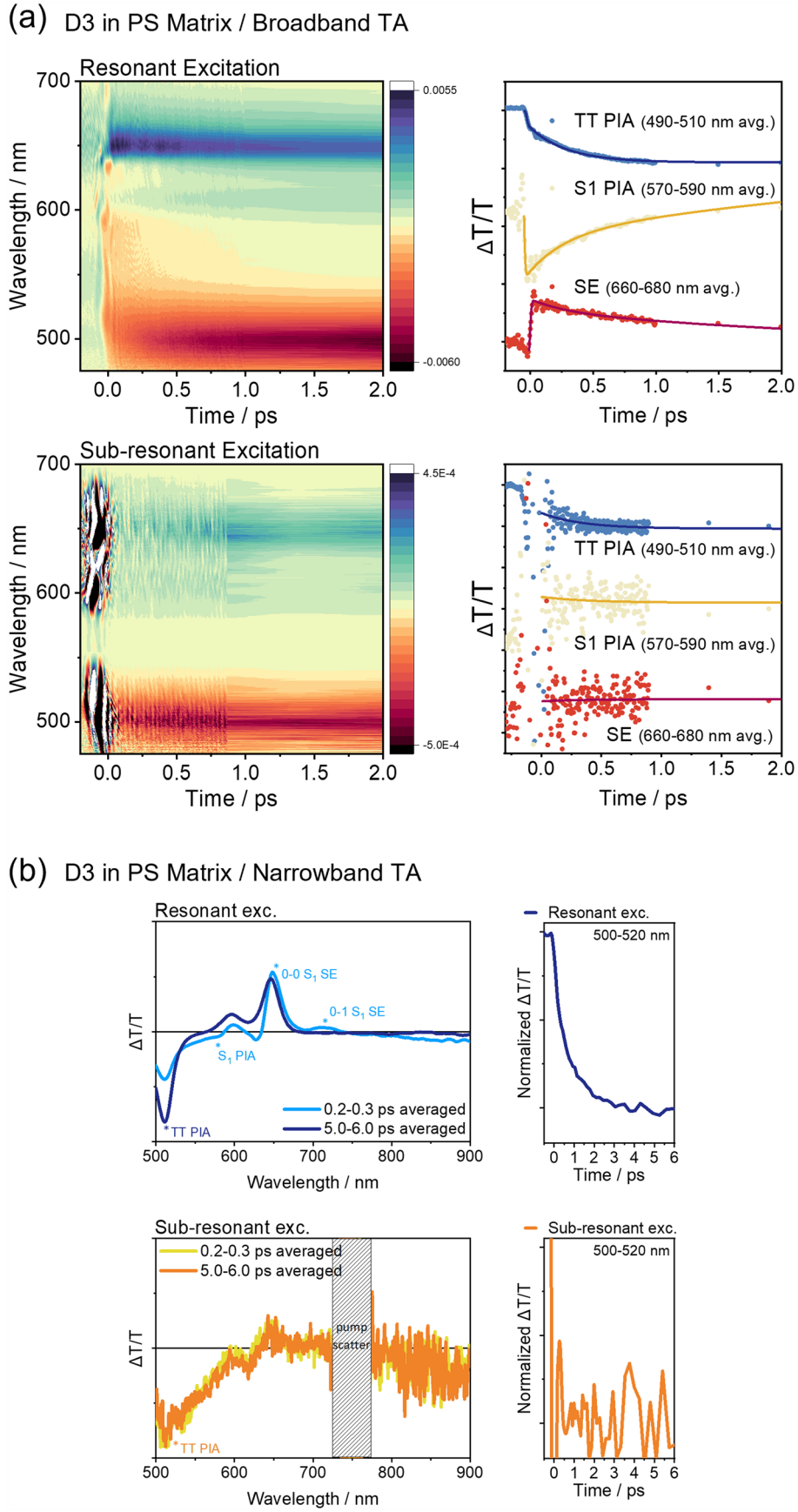

Extended Data Fig. 8 | TA of dimer D3. (a) Broadband ultrafast TA measurements on **D3** in polystyrene matrix. 2D contour maps (left) and temporal profiles (right) are plotted. **(b)** Narrowband TA measurements on **D3** in polystyrene matrix. Representative TA spectra in visible region (left) and decay profiles (right) are plotted.

https://doi.org/10.1038/s41557-024-01556-3

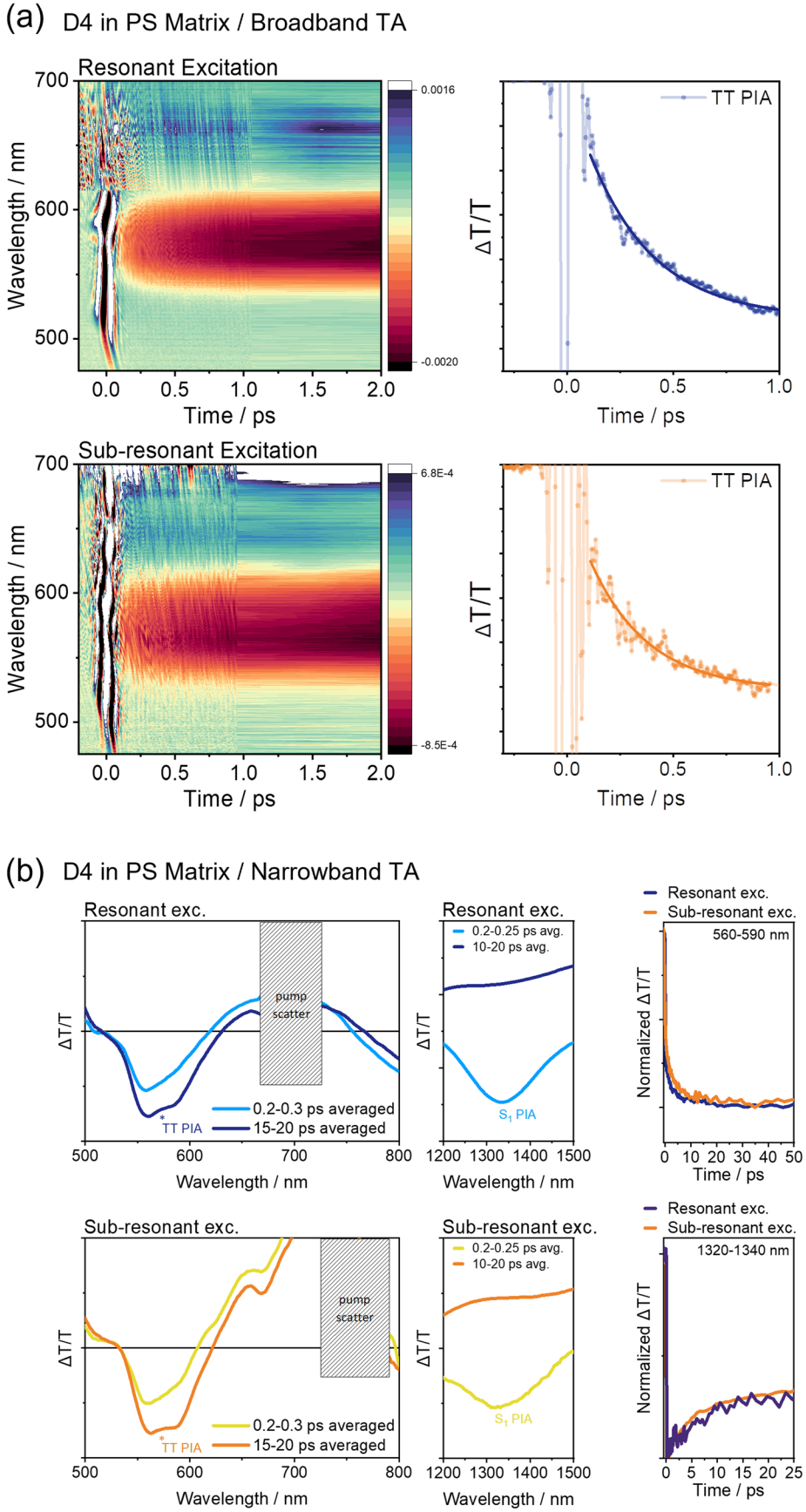

Extended Data Fig. 9 | TA of dimer D4. (a) Broadband ultrafast TA measurements on **D4** in polystyrene matrix. 2D contour maps (left) and temporal profiles (right) are plotted. **(b)** Narrowband TA measurements on **D4** in polystyrene matrix. Representative TA spectra in visible region (left) & near-infrared region (middle) and decay profiles (right) are plotted.

https://doi.org/10.1038/s41557-024-01556-3

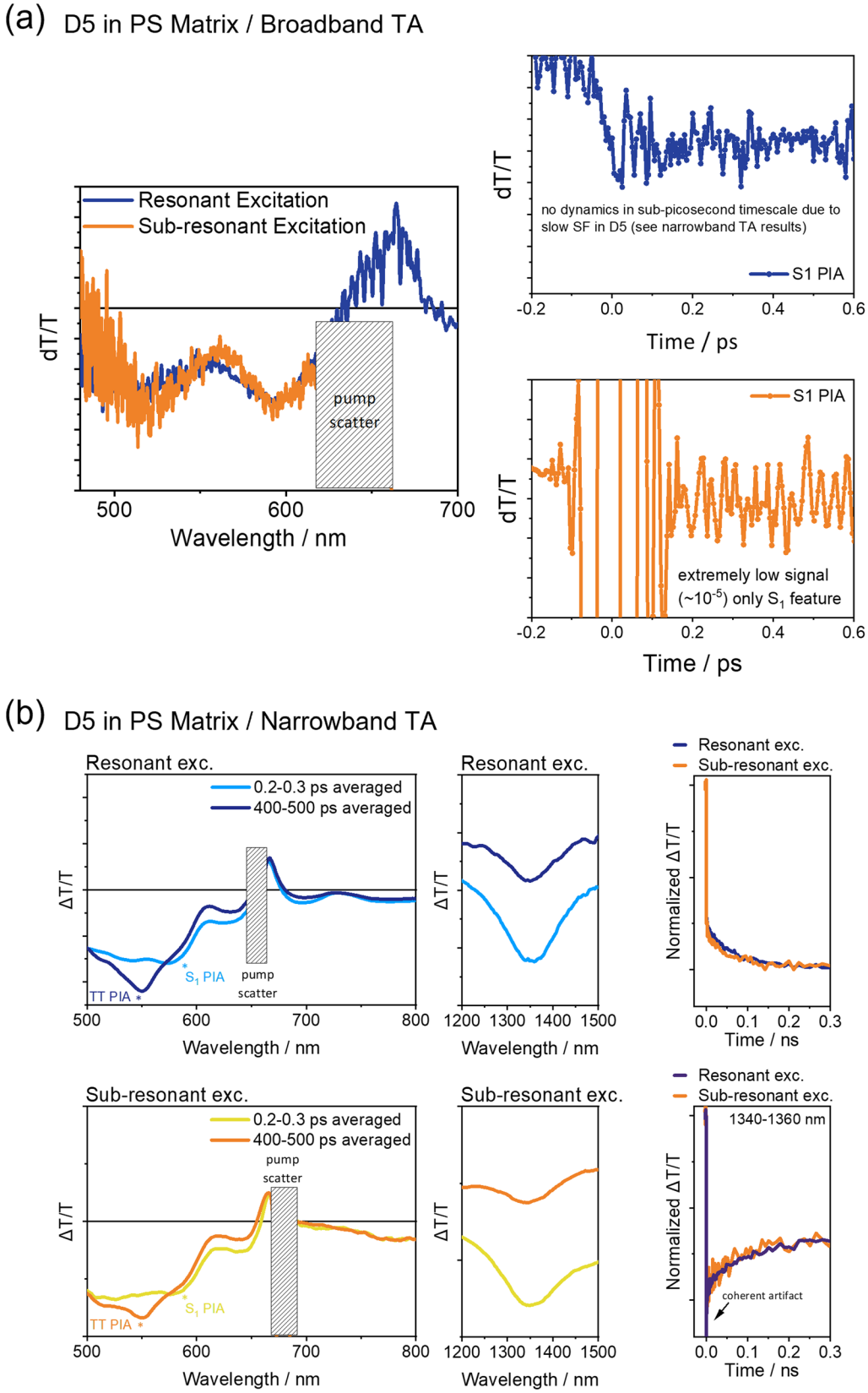

Extended Data Fig. 10 | TA of dimer D5. (a) Broadband ultrafast TA measurements on **D5** in polystyrene matrix. Representative TA spectra (left) and temporal profiles (right) are plotted. **(b)** Narrowband TA measurements on **D5** in polystyrene matrix. Representative TA spectra in visible region (left) & near-infrared region (middle) and decay profiles (right) are plotted.